DOI: 10.1590/2317-4889201620160023

ARTICLE

Mapping iron oxides with Landsat-8/OLI and EO-1/Hyperion imagery from the Serra Norte iron deposits in the Carajás Mineral Province, Brazil

Mapeamento de óxidos de ferro usando imagens Landsat-8/OLI e EO-1/Hyperion nos depósitos ferríferos da Serra Norte, Província Mineral de Carajás, Brasil

Diego Fernando Ducart[1,2*], Adalene Moreira Silva[2], Catarina Labouré Bemfica Toledo[2], Luciano Mozer de Assis[3]

ABSTRACT: Mapping methods for iron oxides and clay minerals, using Landsat-8/Operational Land Imager (OLI) and Earth Observing 1 (EO-1)/Hyperion imagery integrated with airborne geophysical data, were applied in the N4, N5, and N4WS iron deposits, Serra Norte, Carajás, Brazil. Band ratios were achieved on Landsat-8/OLI imagery, allowing the recognition of the main minerals from iron deposits. The Landsat-8/OLI imagery showed a robust performance for iron oxide exploration, even in vegetated shrub areas. Feature extraction and Spectral Angle Mapper hyperspectral classification methods were carried out on EO-1/Hyperion imagery with good results for mapping high-grade iron ore, the hematite-goethite ratio, and clay minerals from regolith. The EO-1/Hyperion imagery proved an excellent tool for fast remote mineral mapping in open-pit areas, as well as mapping waste and tailing disposal facilities. An unsupervised classification was carried out on a data set consisting of EO-1/Hyperion visible near-infrared 74 bands, Landsat-8/OLI-derived Normalized Difference Vegetation Index, Laser Imaging Detection and Ranging-derived Digital Terrain Model, and high-resolution airborne geophysical data (gamma ray spectrometry, Tzz component of gradiometric gravimetry data). This multisource classification proved to be an adequate alternative for mapping iron oxides in vegetated shrub areas and to enhance the geology of the regolith and mineralized areas.

KEYWORDS: Remote sensing; Multispectral and hyperspectral imagery; Iron ore.

RESUMO: *Métodos de mapeamento para óxidos de ferro e argilas, aplicados em imagens Landsat-8/Operational Land Imager (OLI) e Earth Observing 1 (EO-1)/Hyperion e integrados com dados aerogeofísicos, foram testados nos depósitos de ferro de N4, N5 e N4WS, Serra Norte, Carajás, Brasil. Razões de banda foram aplicadas à imagem Landsat-8/OLI, identificando os principais minerais dos depósitos de ferro de N4 e N5. As imagens Landsat-8/OLI mostraram um bom desempenho para a exploração de óxido de ferro, mesmo em áreas vegetadas. Extração de feições espectrais e o método de classificação hiperespectral Spectral Angle Mapper foram aplicados na imagem EO-1/Hyperion com bons resultados para o mapeamento de minério de ferro de alto teor, bem como da proporção de hematita-goethita do minério e de argilas nos regolitos. A imagem EO-1/Hyperion provou ser uma excelente ferramenta para o mapeamento remoto de minerais em áreas de mina a céu aberto, bem como no mapeamento das pilhas de minério. Uma classificação não supervisionada foi aplicada a dados de 74 bandas do visível e infravermelho próximo do EO-1/Hyperion, índice Normalized Difference Vegetation Index derivado do Landsat-8/OLI, Modelo Digital do Terreno derivado do Laser Imaging Detection and Ranging, e dados aerogeofísicos (gamaespectrometria e componente Tzz do dado gravimétrico gradiométrico). Essa classificação de dados multifonte mostrou ser uma alternativa para mapeamento de óxidos de ferro em áreas vegetadas, bem como da geologia do regolito e das áreas mineralizadas.*

PALAVRAS-CHAVE: *Sensoriamento remoto; Imagens multiespectrais e hiperespectrais; Minério de ferro.*

[1]Instituto de Geociências, Universidade Estadual de Campinas – UNICAMP, Campinas (SP), Brazil. *E-mail: diego.ducart@gmail.com*

[2]Instituto de Geociências, Campus Darcy Ribeiro, Universidade de Brasília (UnB), Brasília (DF), Brazil. *E-mail: adalene@unb.br*

[3]Exploração Mineral de Ferrosos, Vale S.A., Centro de Tecnologia de Ferrosos, Nova Lima (MG), Brazil. *E-mail: catarinatoledo@unb.br, luciano.assis@vale.com*

*Corresponding author.

Manuscript ID: 20160023. **Received in:** 02/01/2016. **Approved in:** 06/13/2016.

INTRODUCTION

The Serra Norte plateaus contain world-class iron ore deposits, located in the Carajás Mineral Province (Fig. 1). The deposits have grades higher than 64% Fe, low grades of contaminants (Si, Al, Mn, and P) and reserves of 3,842 million tons (VALE 2015). Some deposits are in production, as the cases of N4, N5, and N4WS. The main ore minerals are hematite with subordinate goethite and magnetite. Other mineral assemblage associated to host rocks includes quartz, kaolinite, gibbsite, smectite, talc, carbonate, and chlorite. The deposits are located on discontinuous ridges and plateaus with lateritic crusts that rise abruptly 200 – 300 m above jungle-covered lowlands (Tolbert *et al.* 1971). The iron ore consists of friable, fine-grained hematite with a granular or platy texture which, in most areas, is covered by an ore canga capping. Hard hematite crops out on the crests of hills and occurs as small lenses and tabular bodies in soft friable ore. Herbaceous and shrub vegetation is found in these plateaus, which contrasts with the dense forest that predominantly covers the lowlands. For this reason, the plateau areas have been referred as clearings by Tolbert *et al.* (1971). Optical remote sensors can detect this geobotanical control (Paradella *et al.* 1997, Almeida *et al.* 2009). However, the ore canga is usually under only small parts of these clearing areas. The topography controls important physiognomic variations, including dominant autochthonous species. Mapping minerals in open pits areas and also under vegetation cover is vital not only for mineral exploration but also for monitoring mine waste deposits, in order to estimate the level of pollutants and to define risk management strategies. One of the best cost-benefit methods for mineral mapping involves the application of remote-sensing data.

Spaceborne remote-sensing data have been widely used to obtain information regarding Earth surface properties. Multispectral and hyperspectral imaging data have been successfully used for mineral exploration to map iron oxides. In arid and semiarid regions, outcropping iron oxide zones are mineralogical conspicuous enough to be detected successfully from spaceborne multispectral and hyperspectral data (White *et al.* 1997, Abdelsalam *et al.* 2000, Farooq & Govil 2013, Feizi & Mansouri 2013). In tropical regions, however, high vegetation density can critically limit the successful application of optical remote sensing for detecting and mapping of iron oxide.

This article aims to analyze different methods for mapping iron oxides in the Serra Norte deposits, using data from Landsat-8/Operational Land Imager (OLI) and Earth Observing 1 (EO-1)/Hyperion sensors, integrated with airborne geophysical data. The used methods should be able to discriminate iron oxides and clay minerals, and provide

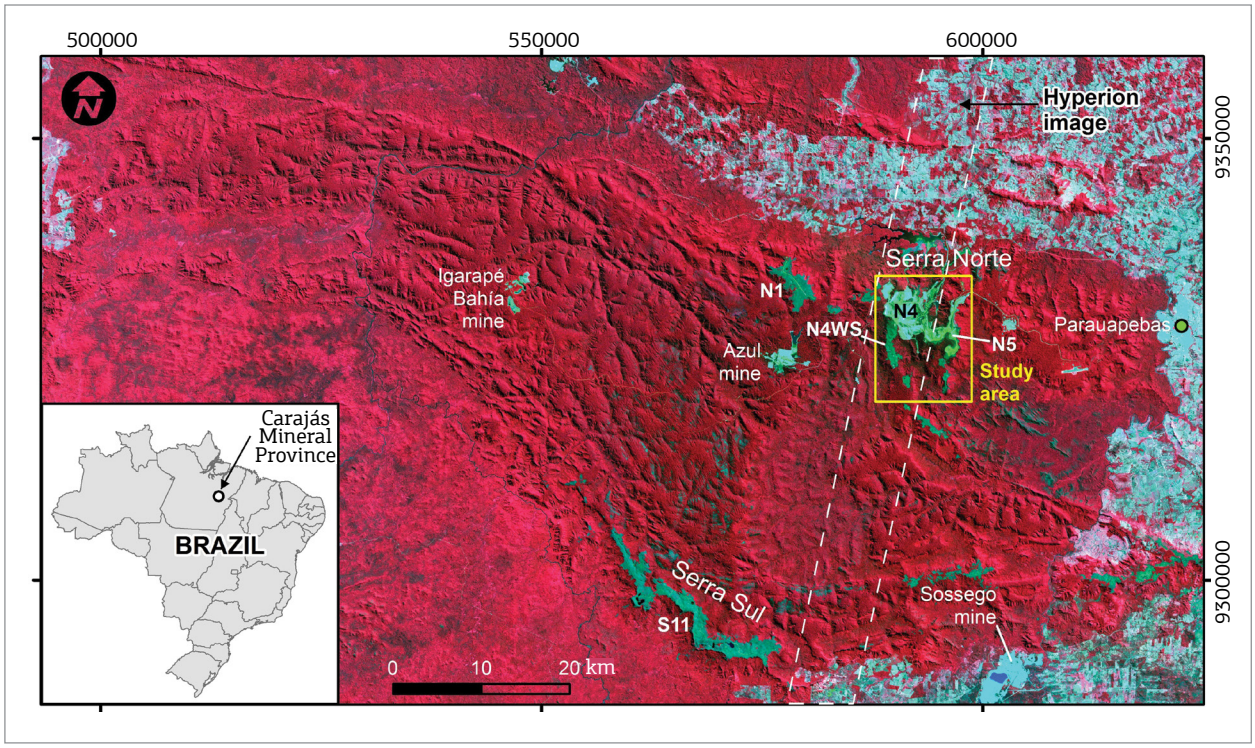

Figure 1. Color composition RGB-432 of Landsat-8/OLI imagery showing the Serra dos Carajás (Pará state) and the study area in the yellow square. The dense forest cover is shown in red. The major mineral deposits are also shown including the iron deposits N1, N4, N5, N4WS (Serra Norte), and S11 (Serra Sul); and the manganese Azul Mine; and IOCG deposits (Igarapé Bahia, Sossego).

semiquantitative mineral information in areas with and without vegetation cover. The hybrid products can contribute to associate bedrock and structural information from depth revealed by geophysical data and their respective signatures on the surface.

GEOLOGY

The study area is located in the Serra dos Carajás, inside the Carajás Mineral Province, Pará state (Fig. 1). The Serra Norte plateaus, where the iron formations occur, were mapped at the scale of 1:20,000 (Fig. 2) by Tolbert *et al.* (1971) and Resende and Barbosa (1972), and updated by Macambira (2003). The geology of the area was recently summarized by Assis (2013) and Prado *et al.* (2016). The region is dominated by metamorphosed volcano-sedimentary sequences and granitoids formed between 2.76 and 2.68 Ga, as well as by the Pium and Xingu Mesoarchean complexes (Cordani *et al.* 1979, Santos 2003, Santos *et al.* 2000, 2006, Tassinari *et al.* 2000, Tassinari & Macambira 1999, 2004).

The Serra dos Carajás is an S-shaped mountain range composed of metamorphosed volcano-sedimentary rocks of the Grão Pará Group, with ages between 2.8 and 2.7 Ga (Gibbs *et al.* 1986, Wirth *et al.* 1986, Olszewski 1989, Trendall *et al.* 1998, Tallarico *et al.* 2003). The lowermost Parauapebas Formation is represented by basalts, basaltic andesites, and basic-to-intermediate pyroclastic rocks (Meirelles *et al.* 1984, Krymsky *et al.* 2002, Macambira & Schrank 2002, Lobato *et al.* 2005). The Carajás Formation, the intermediate portion of the Grão Pará Group, contains layers and discontinuous lenses of jaspilites and iron ore intruded by sills and mafic dikes (Fig. 3B; DOCEGEO 1988). The jaspilites have centimeter thick intercalations of iron oxide, jasper, and chert. The Igarapé Cigarra Formation, at the top of the Grão Pará Group, consists of basaltic flows interlayered with tuffs followed by clastic sedimentary rocks, such as siltstones, phyllites, and greywackes (Gibbs *et al.* 1986, Macambira 2003). Psammopelitic rocks, such as arenites, calcarenites, siltstones, and conglomerates of the Águas Claras Formation, overlay the rocks of the Grão Pará Group.

Lateritic ore canga covers the ore outcrops with thickness up to 20 m. This ore canga has high Fe content and relatively low contaminants, enabling its potential use as an ore. Jaspilite or banded iron formation, with centimeter to millimeter thick laminations or anastomosing pattern, represents the protore and has Fe content ranging between 20 and 40%. The main iron ore is composed of highly friable and porous hematite with 66% average Fe content.

Sterile lateritic regoliths, also called chemical canga, cover mafic rocks or mature and cemented colluvial deposits. Unweathered basalts, gabbros, and diabases are also present. Tuffs are also described but rarer. They occur either as flows or intruded in jaspilites in the form of sills and dykes (Assis 2013).

PHYSIOGRAPHIC ASPECTS AND VEGETATION

The principal physiographic features of this region are the lowlands covered by dense equatorial forest and long, sinuous, and nearly flat plateaus covered by sparse vegetation, commonly underlain by iron formations (Figs. 3A and B). These iron-bearing plateaus are 600 – 700 m in elevation and rise sharply 200 – 300 m above the forested lowlands. The climate is equatorial, with average temperatures ranging between 19 and 31°C, characterized by two distinct seasons, one dry (winter), from May to October, and another wet (summer), from November to April, with very intense torrential rain periods. Predominantly herbaceous and shrub vegetation with little development of semiarboreal type, named as *campo rupestre* (rupestrian field) by Silva *et al.* (1996), is associated with these plateau covers. This vegetation contrasts with the ombrophilous forest that predominantly covers the lowlands – a dense forest characterized by trees exceeding 50 m in height, with a canopy standing out at 25 – 35 m (Fig. 3B).

DATA

Remote sensing data

A cloud-free level 1T (terrain corrected) Landsat-8/OLI imagery (path/row 224/64) was obtained from U.S. Geological Survey Earth Resources Observation and Science Center (USGS-EROS; http://earthexplorer.usgs.gov/). The OLI is a sensor carried by the Landsat 8 satellite, which was launched on February 11, 2013. The performance characteristics of OLI sensor are shown in Table 1. The image used in this study was acquired on August 3, 2013, during the dry season, with 0% cloud cover for the entire scene (Fig. 1). Image processing techniques were applied to the entire scene, but the results are shown in a 125 km^2 subscene on Serra Norte deposits, centred in 6°5'2" S latitude and 50°9'20" W longitude (see yellow square in Figure 1).

The elementary statistics of the spectral Landsat-8/OLI bands, in digital numbers (DNs), are shown in Table 2. The data in the visible bands (1, 2, 3, and 4) have higher minimum values than the data in the near- and shortwave infrared bands (5, 6, and 7). This is due to the Rayleigh atmospheric scattering, affecting mainly

lower wavelengths. The low DNs and standard deviations in the first bands were also a result of this atmospheric effect, as well as the influence of the low vegetation reflectance. The standard deviation progressively increases from bands 1 to 6 as the atmospheric influence decreases and the variation in spectral response of materials and vegetation increases. The notable lower standard deviation of band 7 could be related to the lower energy emitted by the sun in this wavelength, affecting the signal-to-noise ratio (SNR) of the sensor.

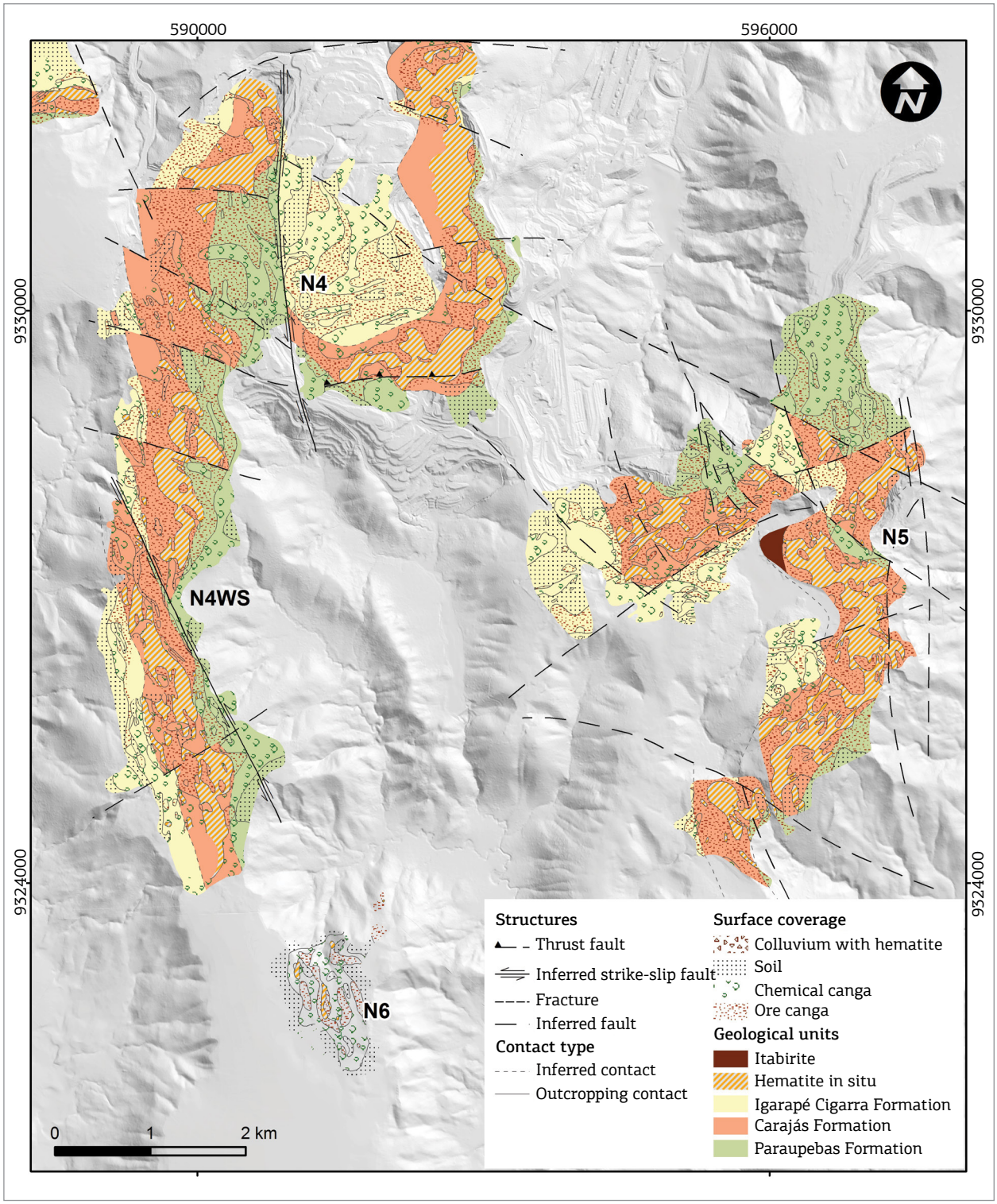

Figure 2. Geological map of the N4, N5 and N4WS iron deposits in Serra Norte (Resende & Barbosa 1972) superposed on a Laser Imaging Detection and Ranging digital terrain model artificially illuminated from northeast.

The Hyperion sensor, carried by the EO-1 satellite, is the first spaceborne hyperspectral instrument to acquire spectral bands in the visible near-infrared region (VNIR) and shortwave infrared region (SWIR) (Pearlman *et al.* 2003). The performance characteristics of Hyperion sensor are shown in Table 1. The SNR of the EO-1/Hyperion sensor is relatively low, between 40 and 190 (Kruse *et al.* 2003), which has a direct effect on spectral mineral mapping, resulting in extraction of less detail. A cloud-free level 1R EO-1/Hyperion imagery (EO1224064209207110PF), obtained from the USGS-EROS, was acquired on July 26, 2009 during the dry season (see EO-1/Hyperion coverage in Figure 1).

Digital elevation models from Laser Imaging Detection and Ranging (LIDAR) data were also used in this study. These data were provided by Vale Company and they cover the entire Serra Norte region. The data were obtained in 2009 and have a linear error of 0.5 m in planimetry and 1.0 m in altimetry. Digital terrain model (DTM) and digital surface model (DSM) were derived from these data. The DTM represents the bare ground surface without any objects like vegetation canopy. The DSM represents the earth's surface and includes all objects on it like vegetation canopy.

Airborne Geophysical data

Assis (2013) used data from Full Tensor Gravity Gradiometry (3D-FTG) airborne geophysical, magnetometric, and gamma spectrometric surveys to map the Serra Norte plateaus and also to generate prospective models. The gamma ray spectroscopy and gravimetric gradiometry airborne data were here integrated with remote sensing

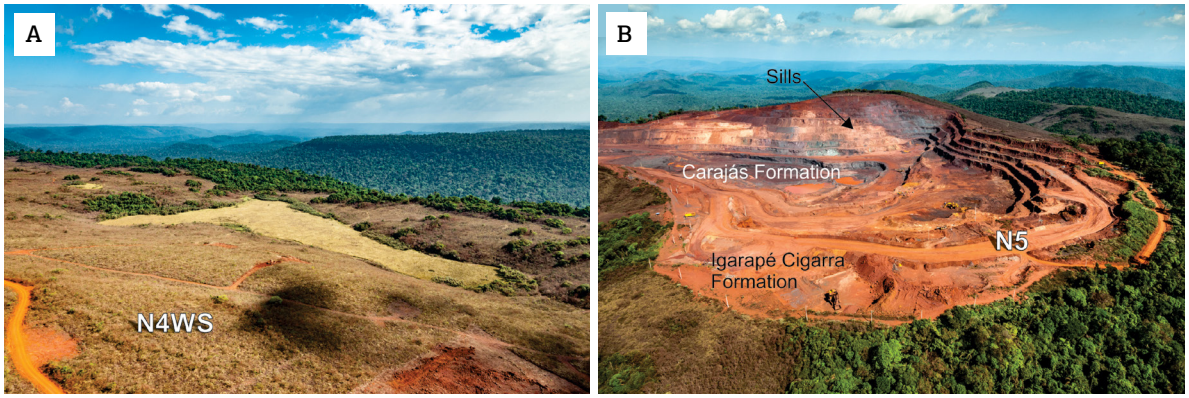

Figure 3. (A) Photograph of N4WS area taken from northeast, showing vegetation clearing over iron deposit and dense forest lowlands in the background. (B) Photograph of N5 mine, showing the Igarapé Cigarra formation above the Carajás formation, and the contrast between the two kinds of vegetation: *campo rupestre* and ombrophilous forest types. Both pictures are courtesy from Vale Company.

Table 1. Performance characteristics of the Landsat-8/OLI and EO-1/Hyperion sensors.

Satellite/ sensor	Subsystem	Band name	Band number	Spectral range (μm)	Spatial resolution	Spectral resolution	Radiometric resolution	Swath width
Landsat-8/ OLI	VNIR	Coastal aerosol	1	0.43 – 0.45	30m	9 bands	16-bits	185 km
		Blue	2	0.45 – 0.51				
		Green	3	0.53 – 0.59				
		Red	4	0.64 – 0.67				
		Near Infrared	5	0.85 – 0.88				
	SWIR	Shortwave Infrared 1	6	1.57 – 1.65				
		Shortwave Infrared 2	7	2.11 – 2.29				
	VNIR	Panchromatic	8	0.50 – 0.68	15m			
		Cirrus	9	1.36 – 1.38	30m			
EO-1/ Hyperion	VNIR		1 – 70	0.36 – 1.06	30m	242 bands	12-bits	7.5 km
	SWIR		70 – 242	0.85 – 2.58				

VNIR: visible near-infrared region; SWIR: shortwave infrared region.

data. A color RGB (KThU) ternary image enhances lateritic covers, iron formation colluvium, and the Igarape Cigarra formation (Fig. 4). This RGB image allowed the identification of signatures associated with outcropping banded iron formations, related to the Carajás Formation through lower levels (dark pixels in Figure 4) of the radioelements K, eU, and eTh (Assis 2013). In general, the regolith signature associated to this unit shows eTh-enriched plateaus. However, the eastern part of the plateau shows high eU that is consistent with iron ore enriched in hematite. The concentration, in this case, reveals an alteration pattern related to the mineralization. The lateritic mantles related to mafic rocks, host rocks of this mineralization associated with Parauapebas and Igarapé Cigarra formations, are eTh- and eU-enriched and show a cyan signature in the RGB-KThU image. Clastic sedimentary rocks such as arkosian sandstones and conglomerates that cover Grão Pará Group showed high levels of K (Assis 2013).

The gravimetric gradiometry data used corresponds to the Z component, obtained from the 3D-FTG aerial survey covering the study area. The 3D FTG system is a mobile platform, inserted in an aerial capsule, and consists of 12 accelerometers equally arranged in three gravity gradient instruments. This equipment measures five independent components of the gravity gradient, Txy, Txz, Tyz, Tzz, Txx, or Tyy. They represent the rate of change of components Gx, Gy, and Gz, which, in turn, represent the gravity acceleration along the Cartesian axes (Murphy 2004). The 3D FTG maps in detail iron formation of the study area in both, surface and subsurface, due to the density contrast in relation to host rocks (Assis 2013). Component Z, called Tzz, maps the mineralized bodies with a high precision (Fig. 5).

METHODS

Spectral characterization of materials

Iron oxides (mainly hematite and goethite) occur in the deforested open-pit N4 and N5 mines. In the VNIR (0.38 – 1.00 μm) of the electromagnetic spectrum, iron oxides have wide absorptions caused by electronic processes: crystal field and charge transfer absorptions (Singer 1981). Crystal field absorption is due to unfilled electron shells of transition elements (Burns 1993), whereas charge transfer occurs where the absorption of a photon causes an electron to move between ions or between ions and ligands (Sherman & Waite 1985). Goethite and hematite have characteristic crystal field absorptions in 0.63 – 0.71 and 0.85 – 1.00 μm, respectively, and an absorption feature caused by charge transfers between 0.48 and 0.55 μm (Fig. 6A; Morris *et al.* 1985). Hunt and Ashley (1979) observed that the abundance of iron (hydro-)oxides is related to the depth of the absorption generated by the crystalline field between 0.85 and 1.00 μm. However, particle size and shape, and physicochemical properties exercise an influence on the spectral absorption (Hunt *et al.* 1971, Morris *et al.* 1985). The most notable change is the overall increase in reflectance or albedo with decreasing particle size for goethite and hematite (Cudahy & Ramanaidou 1997, Ramanaidou *et al.* 2008).

Spectra of main materials found in the study area were obtained from the USGS spectral library (Clark *et al.* 2007; Fig. 6A). These data were validated with field spectral data collected by Prado *et al.* (2016) in drilling cores of the area. The USGS spectra were converted to the spectral resolution of Landsat-8/OLI (Fig. 6B). Iron oxides and vegetation have quite similar reflectance spectra in the wavelength regions covered by Landsat-8/OLI bands 1 and 2, and a small difference in band 3. Vegetation has a peak of reflectance in band 3, but its value is quite similar to that of goethite. In the other hand, hematite has lower reflectance than goethite and vegetation in this band 3. Consequently, these three first bands are not very useful in distinguishing iron oxides in vegetated regions. In the spectral region covered by Landsat-8/OLI band 4, iron oxides (hematite and goethite) and clay minerals have high reflectance and, conversely, the chlorophyll of the green vegetation absorbs strongly radiation at the red wavelengths (band 4). Typical green,

Table 2. Elementary statistics, given in digital numbers, of the spectral bands of Carajás Landsat-8/OLI entire scene without conversion to reflectance.

Sensor	OLI						
Band	**1**	**2**	**3**	**4**	**5**	**6**	**7**
Minimum	7741	7543	6461	5815	4612	4677	4888
Maximum	26328	20204	21226	23576	30466	51002	62905
Mean	9269	8398	7933	7077	17667	12027	8122
StDev	264	352	582	891	1919	2169	1524

moist vegetation shows absorption in band 7 (Fig. 6B), in addition to high reflectance by mesophyll plant tissue in the near infrared (band 5). In the spectral region covered by Landsat-8/OLI band 5, iron oxides show absorption features. Landsat-8/OLI bands 4 and 5 can thus be used to differentiate areas of iron oxides from areas of vegetation. Clay minerals have higher reflectance in spectral region covered by Landsat-8/OLI bands 1, 2, 3, 4, 5, and 6, than those of iron oxide and vegetation (Figure 6B). Clay minerals have an absorption feature in the spectral

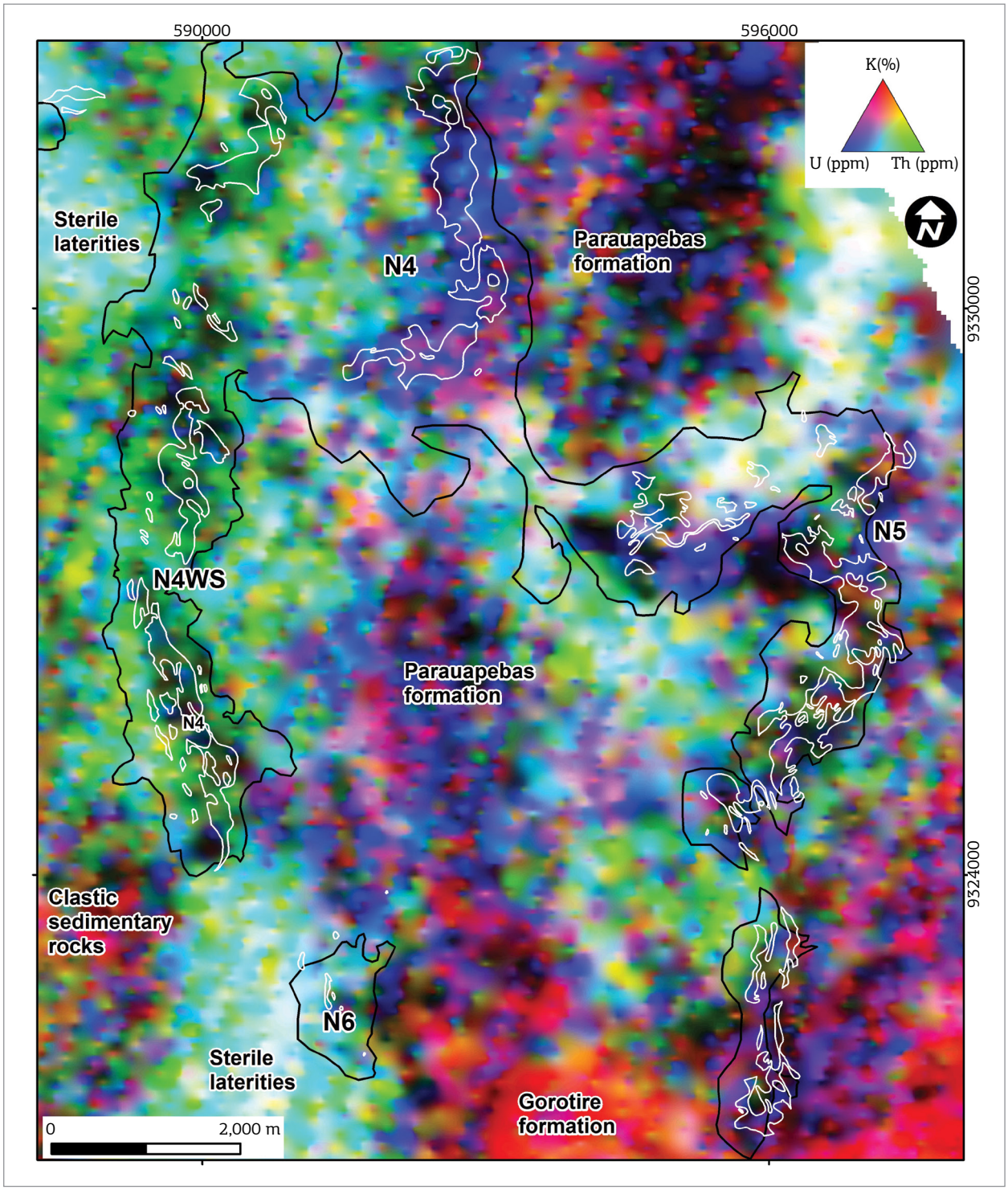

Figure 4. Airborne geophysical data processed by Assis (2013) used in this study. False color composite RGB (KThU) color. Black lines correspond to deposit area, and white lines to outcropping hematite (see hematite *in situ* in Figure 2).

region covered by Landsat-8/OLI band 7, while iron oxides have not any diagnostic spectral feature in the SWIR region. Vegetation has absorption features in the spectral region 2.2 μm (Fig. 6A) produced by biochemical compounds, such as cellulose, lignin, hemicellulose, starch, sugars, and proteins. Spectral regions covered by Landsat-8/OLI bands 6 and 7 are commonly used in the detection of clay minerals (Rowan *et al.* 1974, Goetz & Rowan 1981). However, similarities in shape and relative intensities of the reflectance curves of vegetation and clay

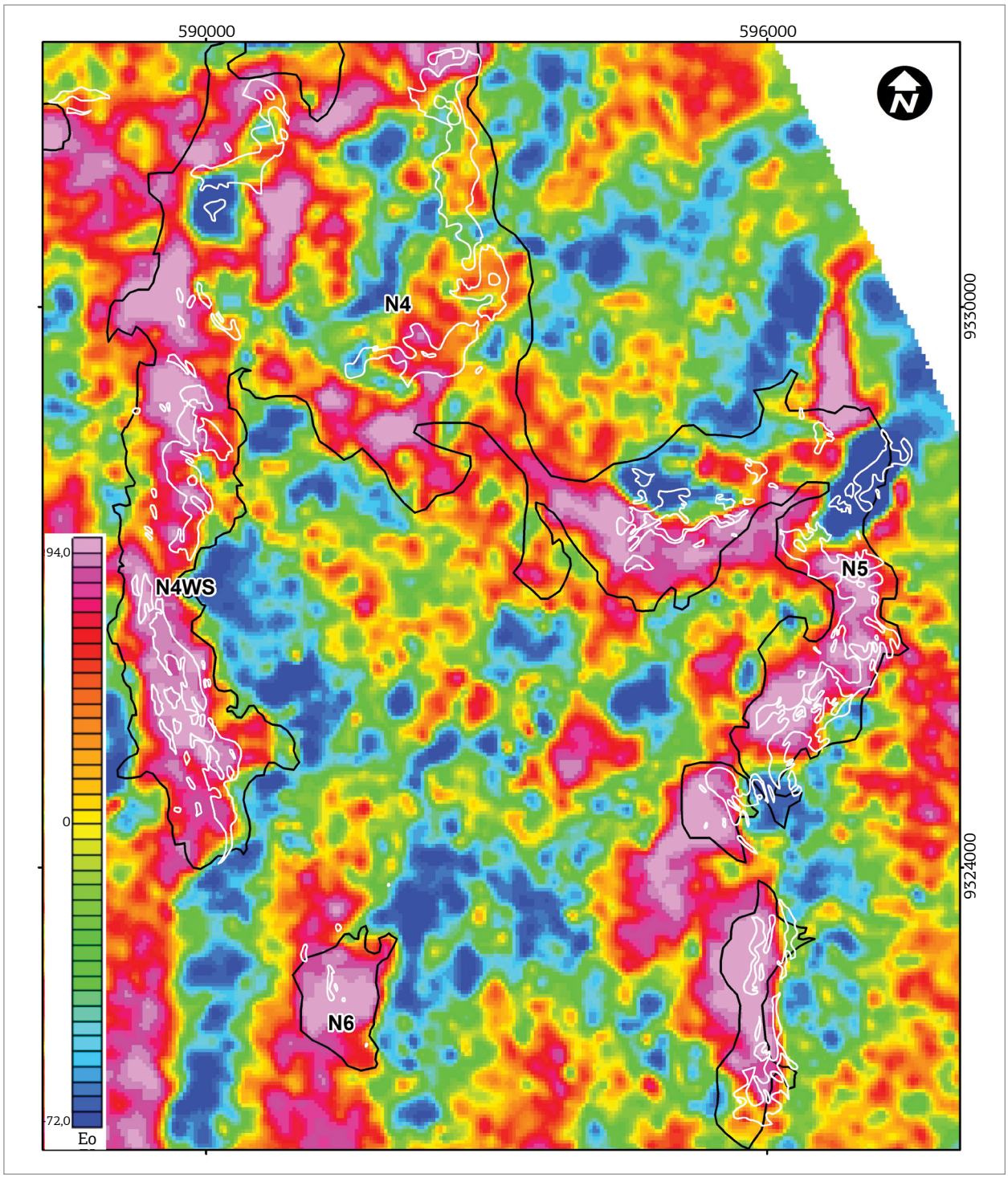

Figure 5. Airborne geophysical data processed by Assis (2013) used in this study. Grids of the Tzz component of the gravimetric gradiometry for a terrain correction with density of 2.67 g/cm³. Scale in Eotvos (Eo). Black lines correspond to deposit area, and white lines to outcropping hematite (see hematite *in situ* in Figure 2).

minerals in the spectral regions covered by Landsat-8/OLI bands 6 and 7 make their differentiation difficult.

Figure 6D shows some reflectance spectra extracted from N4, N5, N4WS, and forest areas (see locations in Figure 6C) of the Landsat-8/OLI reflectance data. Geological map and field reflectance spectra were used for generating training pixels from images. Spectra 2 and 3 are located inside the open pit of the N4 mine. Spectrum 2, located in the high-grade iron ore, is similar to that of hematite shown in Figure 6B. This spectrum shows the highest reflectance difference between Landsat-8/OLI bands 6 and 5, with a high absorption in band 5 as a result of high iron oxide abundance. Spectrum 3 shows a high reflectance difference between Landsat-8/OLI bands 6 and 7, similar to that of

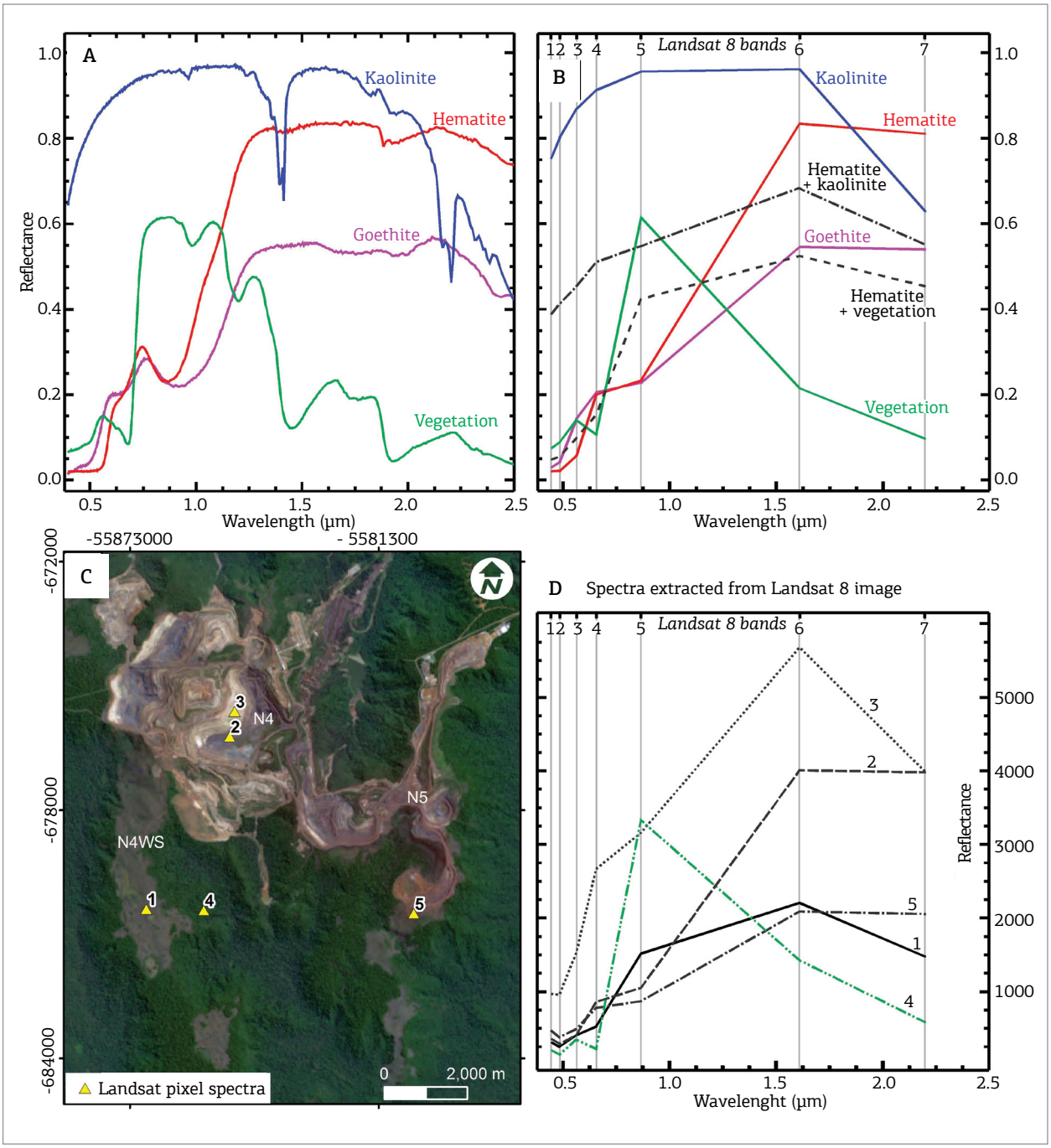

Figure 6. (A) Reflectance spectra from USGS spectral library showing the main minerals found on the surface of Serra Norte deposits. (B) The same reflectance spectra from (A) converted to the spectral resolution of Landsat-8/OLI. Two artificial mixtures are also shown. (C) RGB color composition with Landsat-8 bands 4, 3, and 1, showing the position of pixels, related to the spectra in (D).

kaolinite shown in Figure 6B. This spectrum also shows a mixture with iron oxide, but with less proportion of iron oxide than in spectrum 2 (Figure 6D). Spectrum 5 is similar to hematite or goethite, but also with less iron oxide abundance than previous ones. Spectrum 1, located in the ore canga of the N4WS area, represents a mixture between vegetation and iron oxide. Finally, spectrum 4 is typical of vegetation.

Preprocessing of remote sensing data

Preprocessing applied to Landsat-8/OLI imagery consisted of the following steps: conversion from the original GeoTIFF format to the standard Envi format, conversion to radiance using Envi 5.3 software, and atmospheric correction using the Fast Line-of-sight Atmospheric Analysis of Spectral Hypercubes (FLAASH).

A tropical atmospheric model was used for the atmospheric correction. Figure 7B and C show spectra obtained from a same vegetation pixel of Landsat-8/OLI (Fig. 7A) with and without the atmospheric correction. The spectrum extracted from the image without atmospheric correction (Fig. 7B) shows clearly the effects of atmospheric haze dispersion in the visible bands 1 and 2. The spectrum of the same pixel of the atmospheric-corrected image compares quite well with a vegetation spectrum from the USGS spectral library, except in band 1, where there is a small difference in reflectance caused by haze (Fig. 7C). The Normalized Difference Vegetation Index (NDVI) calculated for the same pixel (Fig. 7A) of the Landsat-8/OLI imagery with and without atmospheric correction gives notably different results (Fig. 7B and C).

With the purpose of masking water bodies in the image, a Landsat-8/OLI band ratio 3/6 was used to highlight areas having a steep decrease in reflectance between the green and SWIR wavelengths (Rockwell 2013). Water is characterized by intense absorption in the SWIR relative to the visible spectral regions. A threshold value for the ratio was chosen based on the examination of standing water in the Landsat scene. This mask was then applied to different results other than the green vegetation index to remove data from areas of standing water.

EO-1/Hyperion data demands careful preprocessing for radiometric and noise correction. From the original 242 EO-1/Hyperion bands, only 155 are calibrated and do not show band overlapping and intense atmospheric absorption (original bands 8 – 57, 79, 83 – 119, 133 – 164, 183 – 184, and 188 – 220). Consequently, these 155 bands were selected for the following processing.

The preprocessing of the EO-1/Hyperion imagery included:

1. conversion from original HDF data format to ENVI format;
2. conversion to radiance;
3. fixing bad detectors cells;
4. column destriping;
5. atmospheric correction;
6. spectral polishing to reduce the spectral artefacts in atmospherically corrected data;
7. identification and masking of spectral outliers, especially pixels containing detector spikes.

This preprocessing was carried out by using Envi, FLAASH, and MMTG/A-Module List (Mason 2002) software. The vertical striping appearing in the VNIR and SWIR

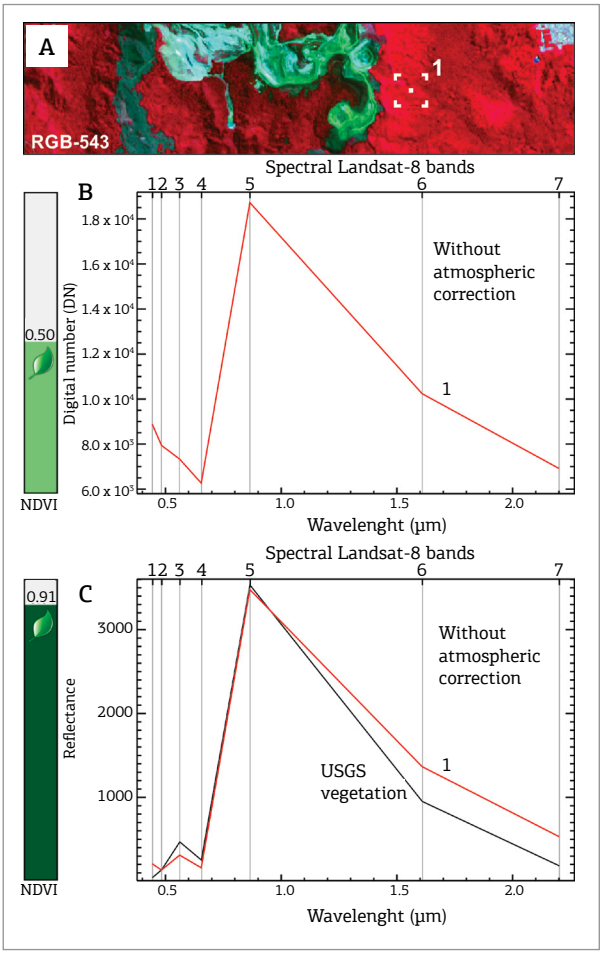

Figure 7. (A) RGB color composition with Landsat-8/OLI bands 4, 3, and 1, showing the position of a pixel (1), related to the spectra of (B) and (C). (B) Spectrum 1 extracted from the image without atmospheric correction. (C) Spectrum 1 from the image with atmospheric correction, compared with a Landsat-8/OLI bandpass-converted and normalized vegetation spectrum from the USGS spectral library. Normalized Difference Vegetation Index values are shown on the left of (B) and (C) for the same pixel.

bands of EO-1/Hyperion data is common to all pushbroom type sensors, albeit quite severe in Hyperion data, and it is due to miscalibration of the area detector array. The striping was corrected by using the "Pushbroom Destriper" (MMTG/A-Module List), which uses the histogram statistics (mean and standard deviation) of the column pixels of each band to balance them with the statistics of all columns of the complete image. The effects of stripping and its correction on EO-1/Hyperion 155 bands were tested using the Maximum Noise Faction (MNF) transformation (Green *et al.* 1988; Fig. 8A and B). MNF transformation can be an effective tool for assessing the quality of hyperspectral images (Datt *et al.* 2003). The correction results showed a significant reduction of the striping over the original image.

The atmospheric correction was carried out using the tropical atmospheric and rural aerosol models. Pixel-based estimate of water vapor was measured using the continuum depth of the 1.135 μm band. The efficacy of the atmospheric correction was assessed through the recognition of green vegetation spectral signatures on dense forest (Fig. 9). The overall shape, including the characteristic NIR plateau between 0.700 and 1.300 μm, as well as absorption bands related to chlorophyll (0.675 μm) and leaf water (0.990, 1.190 μm) are clearly evident in the corrected EO-1/Hyperion data. There is still a noncorrected haze effect in the first bands of the atmospheric-corrected image (Fig. 9).

The FLAASH module also corrected the smile effect, which is another common problem encountered in Hyperion data. This effect is due to a shift on the central wavelength of the pixel through the imaging direction line (cross-track), which results from the curvature of the detector entrance slit (Goodenough *et al.* 2003). This effect can be detected by using the MNF band 2, which is observed in an abnormal brightness gradient (Fig. 8C and D).

Processing of EO-1/Hyperion and Landsat-8/OLI imagery was carried out using mainly ENVI 5.3 software, including band ratios, SAM method, and ISODATA unsupervised classification. The "Spectral Indices" tool of the software MMTG/A-Module List was used for feature extraction on VNIR 74-bands of Hyperion image.

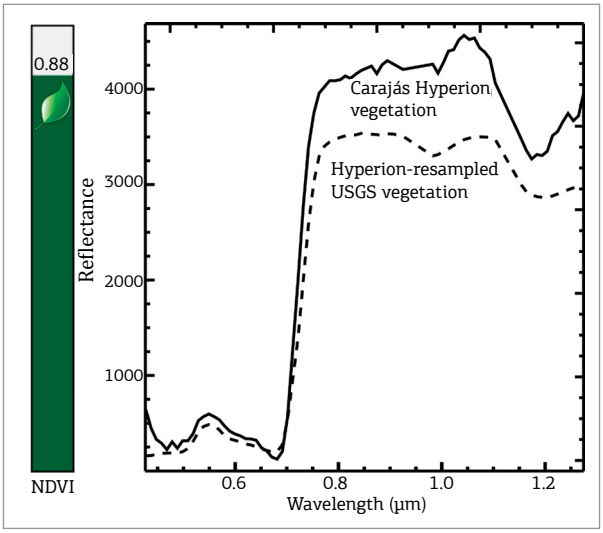

Figure 9. Spectrum extracted from EO-1/Hyperion imagery corresponding to a dense vegetation area, compared with a bandpass converted and normalized vegetation spectrum from USGS spectral library.

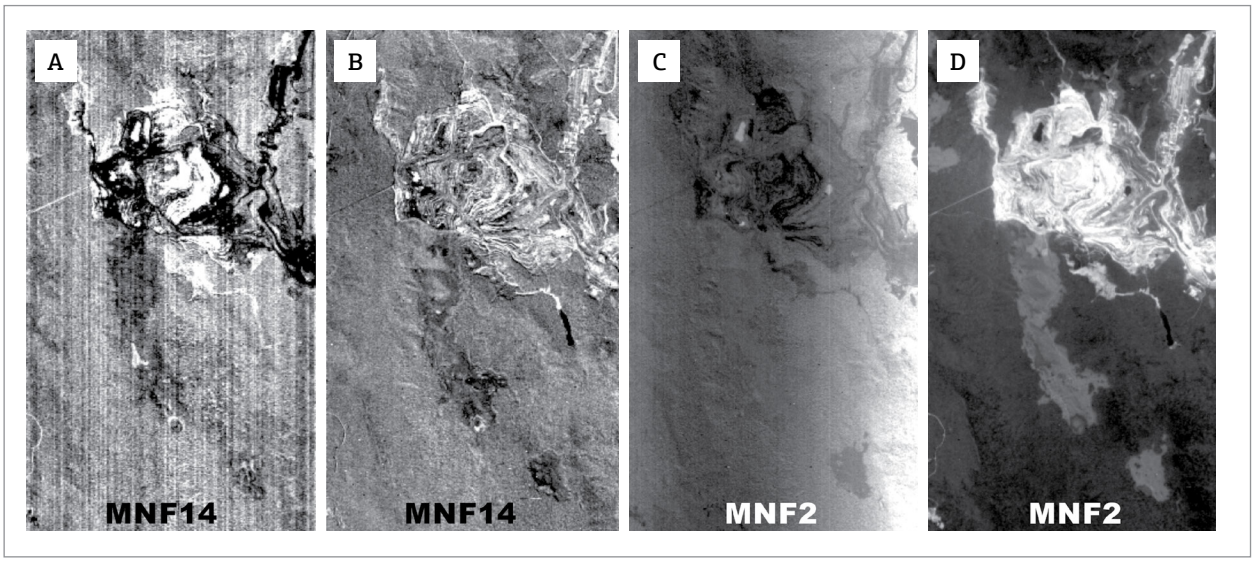

Figure 8. Maximum Noise Faction (MNF) transformation applied on EO-1/Hyperion 155 bands with and without radiometric corrections. (A) MNF band 14 resulting from original image showing the striping problem. (B) MNF band 14 resulting from destriped image. (C) MNF band 2 resulting from the original image showing the smile and striping effects. (D) MNF band 2 resulting from destriped image with atmospheric correction.

PROCESSING AND RESULTS

Band Ratios applied to Landsat-8/OLI

Spectral band ratios were carried out to Landsat-8/OLI bands to detect groups of minerals with strong absorption bands at similar wavelengths. The results of band ratios were integrated in a class image (Fig. 10).

The first group is typified by ferric iron minerals (including hematite and goethite), which have absorptions in the bands 2 and 5, and high reflectance in bands 4 and 6 (Fig. 6B). Two Landsat-8/OLI band ratios were tested to highlight ferric iron-bearing zones in the study area:

1. band ratio 4/2;
2. band ratio ((4+6)/5).

High values in band ratio 4/2 are useful to detect the charge transfer absorption related to ferric iron oxides in the blue spectral region. The ratio is sensitive to ferric iron even in low concentrations. High values of this band ratio highlighted iron oxides related to mafic regolith, but not the high-grade iron ore (see Iron Oxide class in Figure 10).

High values of band ratio (4+6)/5 are useful to detect the crystal-field absorption of ferric iron oxide in the band 5 (Rockwell 2013). The results of this band ratio highlighted mainly the high-grade iron ore and, secondarily, iron related to the mafic saprolite. The results of this ratio correlate with the high-grade iron observed at the bottom of N4 and N5 open pits and in the iron ore stockpile of the railway loop (see High Grade Iron Ore class in Figures 10 and 11). The second group is characterized by a strong absorption feature near 2.2 – 2.3 μm in band 7, and includes hydroxyl-bearing minerals (for example, clay and mica minerals), hydrated sulfates (for example, gypsum and alunite), and, less intensely, carbonate minerals (calcite and dolomite). In the study area, only kaolinite is present at surface, which is formed by laterization processes. Band ratio 6/7 is commonly used with for its ability to map clay minerals (Knepper 1989). However, vegetation spectra also have a high reflectance on band 6 and low reflectance in band 7 (Fig. 6B). Consequently, a simple band ratio 6/7 enhances not only clays but also vegetation (Agar & Coulter 2007). Band ratio 5/4 highlights areas of green vegetation with abundant chlorophyll content (see Vegetation class in Figure 10). Results of the Landsat-8/OLI band ratio 6/7 were divided by the ratio 5/4 to generate the clay index. It shows clays in areas related to mafic regoliths. In N4 open-pit area, these clays are related to the Igarapé Cigarra Formation, clearly over the Carajás Formation with high-grade iron ore (Fig. 11). As this result superposes those of iron oxide ratio 4/2, a mixed class is generated: Clays + iron oxide (Fig. 10). Superposing vegetation and iron oxide ratio 4/2 is registered in the class Iron oxide + vegetation.

The NDVI was also applied to the Landsat-8/OLI imagery. NDVI is a standardized vegetation index, which generates an image showing an estimation of biomass. NDVI and other simple near-infrared/red band ratios are affected by external factors such as the state of the atmosphere, illumination and viewing angles, soil background reflectance, and canopy architecture (Mather 1999). The rainbow-colored NDVI image shows the dense forest in red and orange, the mixture of sparsely vegetated and iron oxides of N4WS and N6 areas in yellow and light yellow, the bare soil and outcropping iron oxides of N4 and N5 open pits in light blue, and the water in dark blue (Fig. 12).

Feature extraction applied to EO-1/ Hyperion imagery

Iron oxide abundance and hematite–goethite ratio spectral parameters were obtained from the polynomial curve that best fits the reflectance spectrum for which the continuum was removed. For this purpose, the following absorption band parameters calculated from continuum removed spectra were used in this study: the absorption band position and the absorption band depth. The absorption band position is defined as the wavelength at which the polynomial curve that adjusts the absorption feature reaches the reflectance minimum of the curve. The depth of the absorption feature was calculated using the method proposed by Clark and Roush (1984), subtracting the minimum reflectance value of the polynomial curve of the reflectance value of the continuum at the same wavelength and then dividing this value by the reflectance of the continuum. The polynomial fit approach to the spectral feature smoothes out some of the effects of noise in the data and is not affected by overall band shape (Cloutis *et al.* 1986). When the absorption feature is not present in the analyzed spectrum, the depth value is equal or close to zero, indicating the absence of the investigated mineral.

Townsend (1987) observed that the position of the Fe^{+3} absorption varies from ~0.86 μm for pure hematite samples to ~0.92 μm for pure goethite samples. These minima absorptions were determined visually from spectra without continuum removal correction. When the continuum removal by division is applied, the position of the minimum is modified by a slope effect (Clark 1999). Consequently, the wavelength position of hematite and goethite ranges from ~0.90 μm for pure hematite to ~0.96 μm for pure goethite in continuum removed spectra. In this study, the depth and position of the iron oxide absorption feature were calculated from a third-degree polynomial curve, fitted to the continuum removed reflectance EO-1/Hyperion spectra (Table 3). The results from this feature extraction are shown in Figure 13A and B. The iron oxide abundance

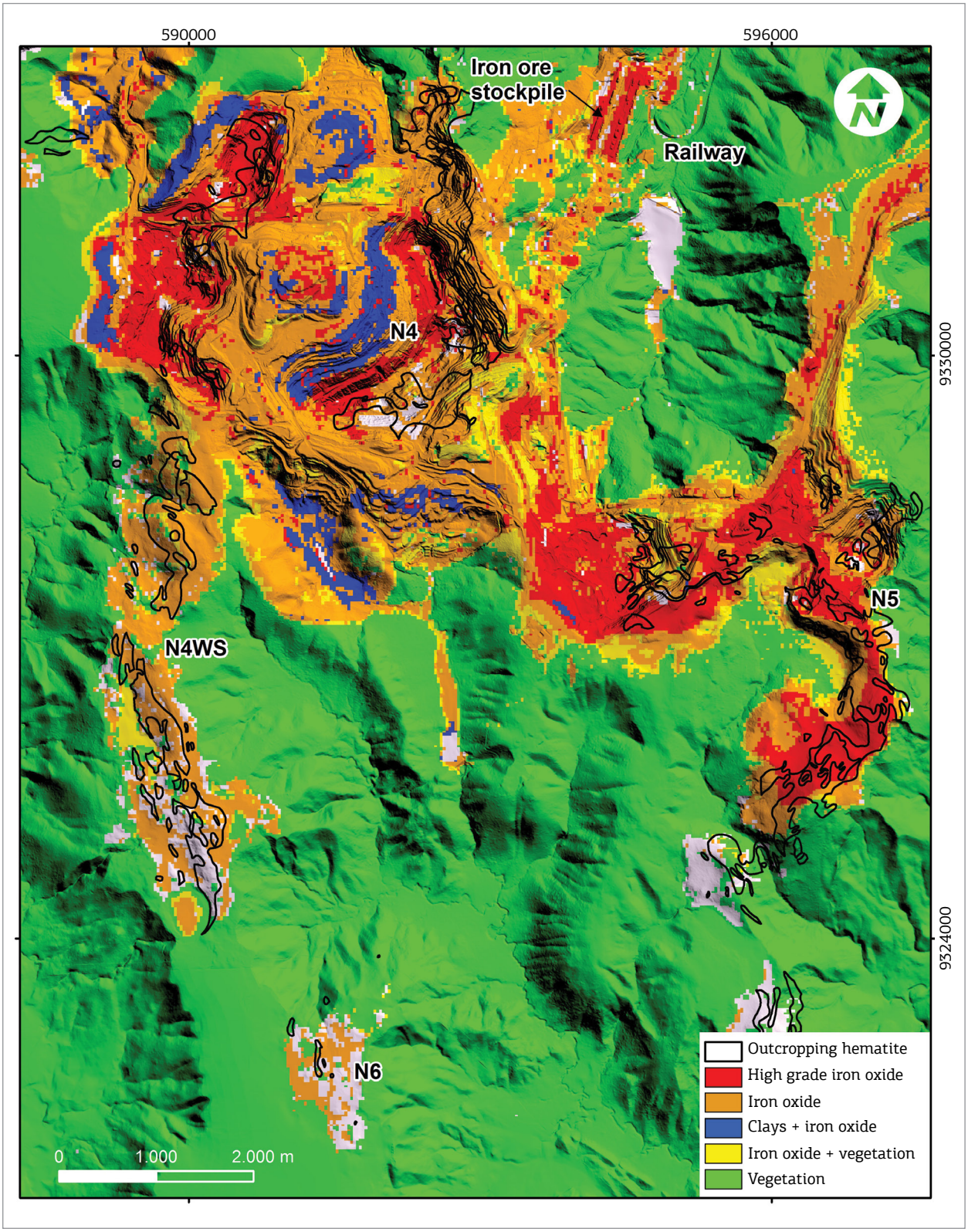

Figure 10. Class image generated from band ratio results applied in Landsat-8/OLI, superposed on a Laser Imaging Detection and Ranging digital terrain model artificially illuminated from northeast. Gray is not a class and corresponds to areas mapped by any band ratio. The continuous black line represents the "hematite *in situ*" unit of Figure 2. Note that this unit corresponds to a map published in 1972 (Resende & Barbosa 1972) before the N4 and N5 open pit beginning construction, and the Laser Imaging Detection and Ranging digital terrain model and Landsat-8/OLI are from 2009 and 2013, respectively, after its construction.

correlates with high-grade iron ore in N4 open-pit area (Fig. 13A). This is also validated with iron oxides laid in the iron ore stockpiles. N5 deposit is outside the EO-1/Hyperion coverage. Because of the influence of spectral response of the grass over the ore canga, no iron oxides were detected in the N4WS deposit. Hematite is the main oxide present in N4 (Fig. 13B), and only small areas of mixtures between hematite and goethite are observed mainly in mafic laterites. This observation is consistent with results reported by Prado *et al.* (2016). Reflectance spectra extracted from EO-1/Hyperion imagery (VNIR region) can be validated with hematite and goethite of USGS spectral library (Fig. 14).

Spectral Angle Mapper method applied on EO-1/Hyperion Imagery

Unsupervised classification

The Iterative Self-Organizing Data Analysis Technique (ISODATA) (Tou & Gonzalez 1974) is an unsupervised classification method commonly applied to satellite images. Spectral reflectance from multiple bands is used to determine clusters in multidimensional attribute space. Multispectral and hyperspectral images are commonly used for classification. The addition of other "bands" or external data measured in a continuous scale, such as digital elevation models or geophysical data, can increase the number of features available for classification. In this study, we applied the ISODATA method to a data set conformed by data from EO-1/Hyperion VNIR 74

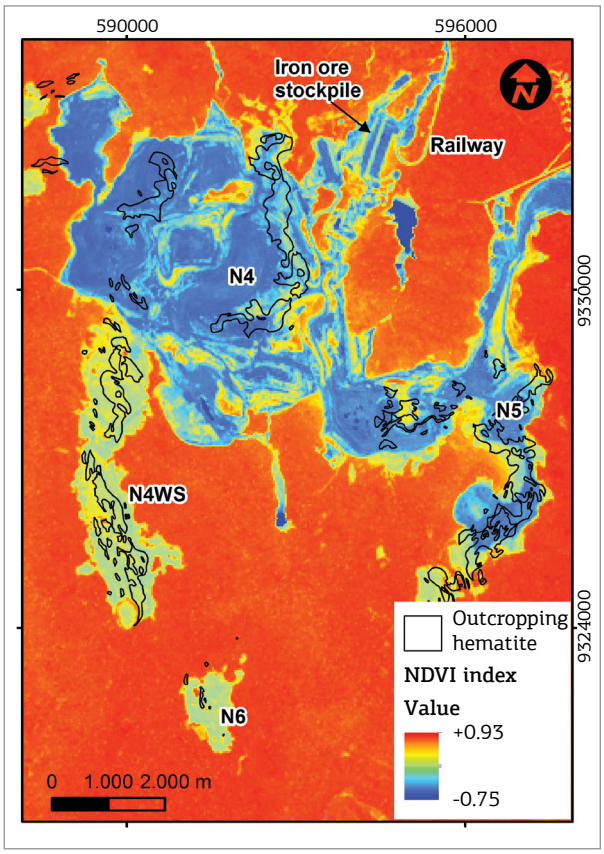

Figure 12. Rainbow-colored Normalized Difference Vegetation Index image generated from Landsat-8/OLI data, showing the vegetation abundance. The continuous black line represents the "hematite *in situ*" unit of Figure 2. Observe the relationship of vegetation in the plateaus.

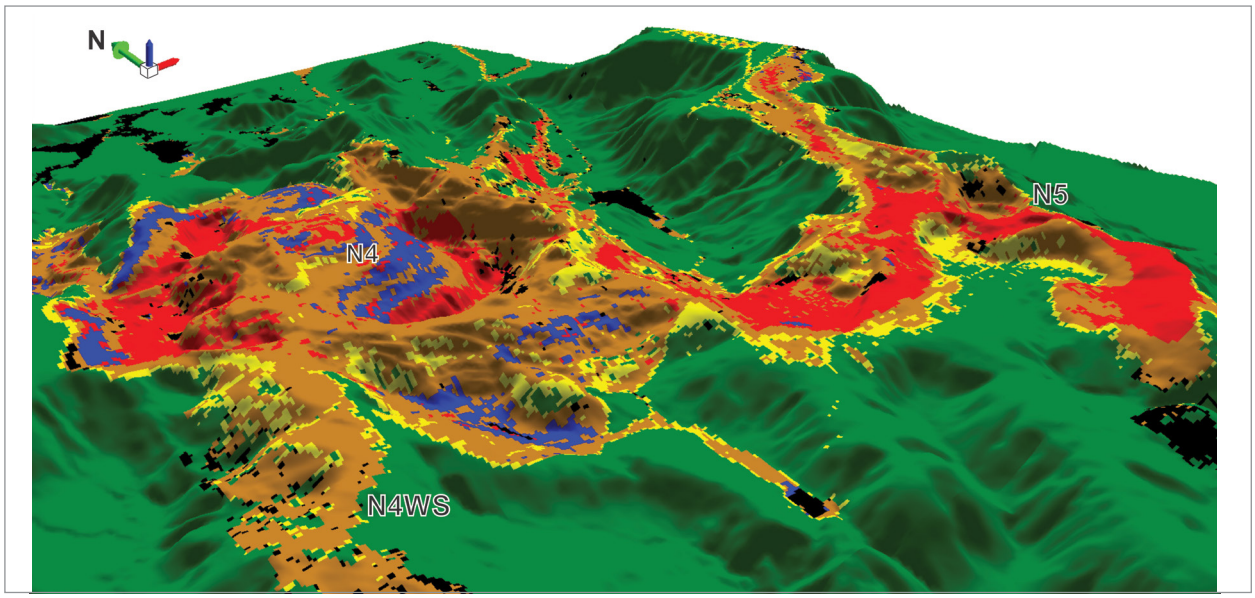

Figure 11. 3D model of the same class image from Figure 10, created with the Laser Imaging Detection and Ranging digital terrain model and artificially illuminated from northeast. Black areas are not a class and correspond to areas mapped by any band ratio.

Table 3. Algorithms applied on EO-1/Hyperion imagery for the extraction of depth and wavelength from 0.90 µm spectral absorption feature of iron oxide.

Image	Product	Function	Base algorithm	Algorithm detail	Filter/ mask
Hyperion VNIR bands	Fe^{+3}abund	Abundance of iron oxides (hematite, goethite)	$900D_{Hyp}$	Depth of the continuum removed spectral feature calculated using a third-degree polynomial from 0.75 – 1.25 µm, with a focus ranging between 0.80 – 1.02 µm	
	Hem-Goet ratio	Differentiate hematite-goethite	$900Wv_{Hyp}$	Wavelength of the continuum removed spectrum calculated using a third-degree polynomial from 0.75 – 1.20 µm, with a focus ranging between 0.80 – 1.05 µm	$900Wv_{Hyp}$ between 0.86 and 0.95 µm

VNIR: visible near-infrared region.

bands, LIDAR-derived DTM, gamma ray spectroscopy, Tzz component of gravimetric gradiometry, and Landsat-8/OLI-derived NDVI. The selection of these data for the classification was based on their own significance in the discrimination of outcropping iron ore. All data were resampled to 30 m, histogram stretched, converted to 8 bits, integrated in a unique layer stack image (containing 78 bands), and spatial subset to an area of 310 ′ 613 pixels. The ISODATA was set up with a number of 50 maximum interactions, 5% of change threshold and 5 minimum pixels per class. The resulting classification image is shown in Figure 16. The results were analyzed considering the knowledge of the phenomenon in question to interpret the significance of the various clusters. The classes with the best visual correspondence with known features described earlier were evaluated.

The ISODATA classification produced seven classes over the main iron deposits (3, 4, 6, 7, 13, 14, and 15) and six classes over the dense forest (5, 8, 9, 10, 11, and 12). Classes 1 and 2 correspond to small water bodies. The significance of the classes over the dense forest was not determined because of the lack of information about different tree species, as well as the geology under this vegetation. In consequence, different tones of green were assigned to the six classes. Classes 3, 4, and 15 are related to areas of high-grade iron ore in the open pit of N4 and in the stockpiles. These classes are correlated with the Carajás Formation in N4 area (Fig. 2). The spectral data derived from EO-1/Hyperion VNIR 74 bands had a large weight on this cluster, with less proportion of gamma ray spectroscopy and Tzz component of gravimetric gradiometry. Class 6 is also related to areas of high-grade iron, but in areas of N4WS plateau. Since this area is covered by rupestrian field vegetation, the NDVI data, together with gamma ray spectroscopy and gravimetric gradiometry data, had a large weight on this cluster. Class 7 discriminates mainly rupestrian field vegetation over lateritic capping related to mafic rocks in plateaus. DTM, gamma ray spectroscopy, and NDVI data had a large weight on this cluster. Mafic saprolites from Igarapé Cigarra Formation in N4 area were discriminated in Classes 13 and 14. Hyperion data and, in less proportion, gamma ray spectroscopy had a large weight on this cluster.

DISCUSSION AND CONCLUSION

This study demonstrates the importance and advantages of the combined use of Landsat-8/OLI and EO-1/Hyperion remote-sensing data, integrated with airborne geophysical data in mineral mapping associated with iron deposits in the equatorial region at Carajás Mineral Province, Brazil. Iron oxides and clay minerals associated to the Serra Norte iron deposits have been detected using this approach. In the N4 and N5 open-pit areas, the band ratio method applied on Landsat-8/OLI imagery proved to be adequate for remote mapping of iron oxides and/or clay minerals. Specifically, band ratio (4+6)/5 showed the best results for mapping high-grade iron ore in N4 and N5 areas. Band ratio 4/2 correctly highlights iron oxides mainly related to mafic saprolites from Igarapé Cigarra Formation in N4 and N5 areas, and also iron oxides under vegetation cover in N4WS area. The result of the Landsat-8/OLI band ratio 6/7 divided by the ratio 5/4 produced an adequate index for detection of clay minerals. Differences between ore canga and chemical canga were not detected in the sparse vegetated N4WS area.

Results obtained from processing hyperspectral EO-1/Hyperion data to map iron oxides and clays were comparable with those of Landsat-8/OLI. The feature extraction and SAM methods applied on EO-1/Hyperion imagery produced acceptable results for mapping high-grade iron oxides,

the hematite-goethite ratio, and clay minerals in N4 and N5 areas. However, the remote detection of iron oxides was rendered difficult in heavily or sparsely vegetated areas, because vegetation obscures the reflectance characteristics of the underlying substrate.

Despite the low SNR and large amounts of noise and artefacts that complicate the preprocessing, EO-1/Hyperion imagery proved to be an excellent tool for fast remote mineral mapping in open-pit areas, as well as for environment monitoring of the mine waste deposits. The Landsat-8/OLI imagery, with a relatively easy preprocessing, showed a solid performance for iron oxide exploration, even in vegetated areas.

Geophysical data provide information about iron ore in subsurface, at different depth levels, whereas remote sensing supplies information from the surface including the vegetation cover. In a general way, the clusters determined by the ISODATA classification produced an acceptable correlation with classes mapped with band ratios (Fig. 10) and feature extraction (Fig. 13A) mainly in the N4 area. However, the ISODATA classification gave superior results in the N4WS area, discriminating an area that has a broad correlation with the high-grade iron deposit (see "hematite *in situ*" in Figure 2). The integration of remote sensing with geophysical data in an unsupervised classification proved to be an adequate alternative to mapping iron oxides in vegetated areas.

ACKNOWLEDGMENTS

We gratefully acknowledge Vale Company for allowing the use of geological and geophysical data and access to the Serra Norte deposits, as well as the research funding through the project *Geração de Modelos Prospectivos para o Minério de Ferro na Província Mineras de Carajás*, supervised by Dr. Adalene Moreira Silva. D.F. Ducart grants the Universidade de Brasília and the Coordination for Improvement of Higher Education Personnel (*Coordenação de Aperfeiçoamento de Pessoal de Nível Superior* – CAPES) for his post-doctoral fellowship through its National Program

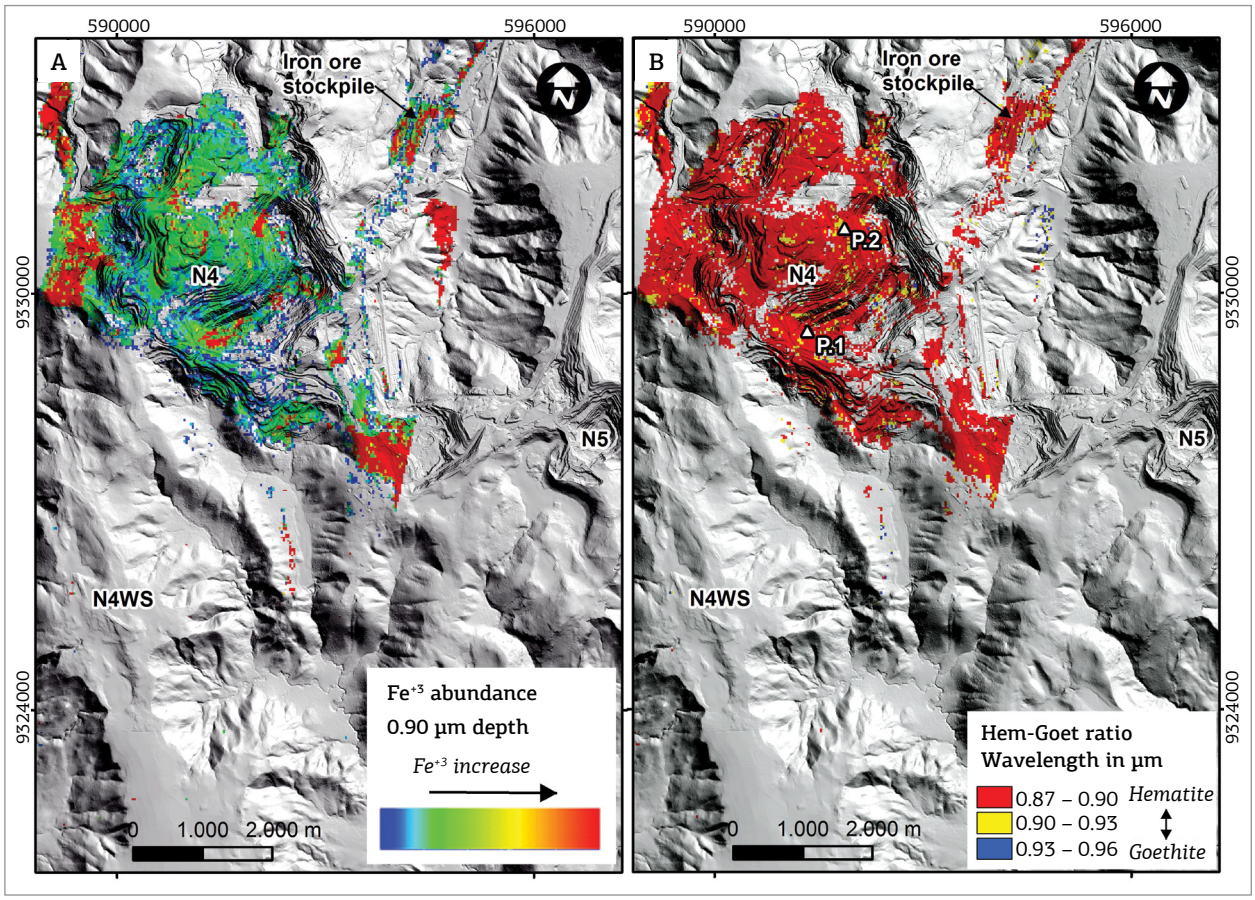

Figure 13. (A) Iron oxide abundance (Fe^{+3}abund) image resulting from extraction of ~0.90 µm absorption depth in EO-1/Hyperion imagery. (B) Hematite-goethite ratio image resulting from extraction of ~0.90 µm absorption wavelength in EO-1/Hyperion imagery. The base for both images is a Laser Imaging Detection and Ranging digital terrain model artificially illuminated from northeast. Note that N5 area is outside the EO-1/Hyperion coverage.

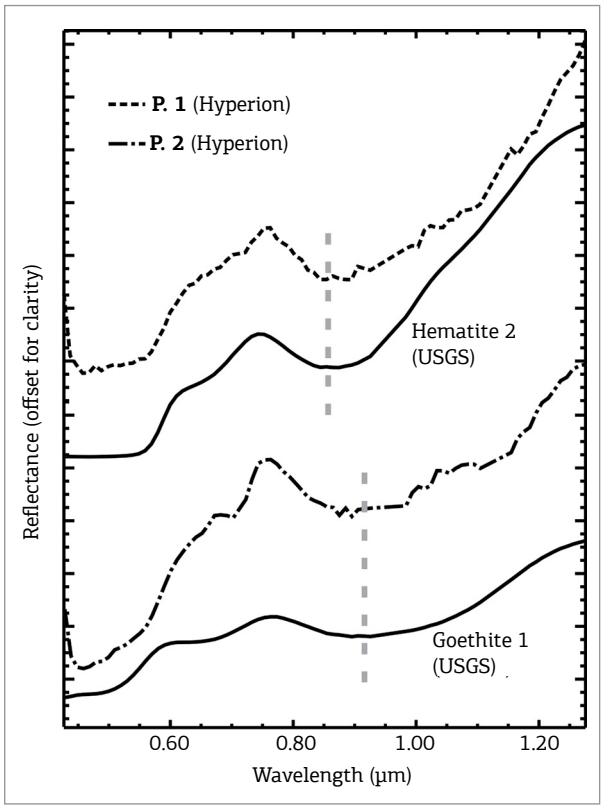

Figure 14. Spectra extracted from EO-1/Hyperion imagery points 1 and 2 (see location in Figure 13B), compared with hematite and goethite spectra from the USGS spectral library.

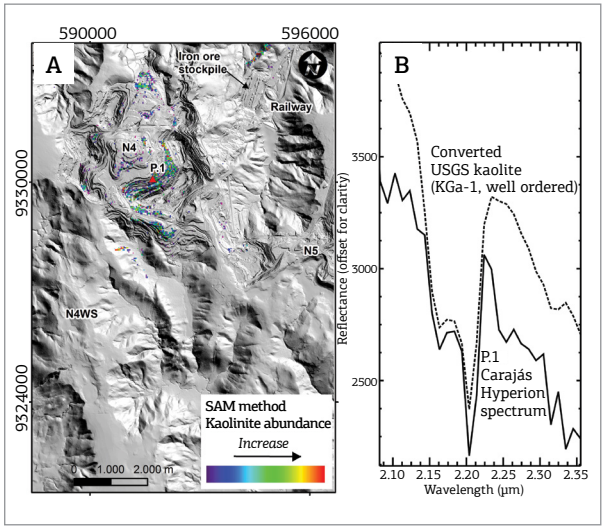

Figure 15. (A) Kaolinite abundance image (in rainbow color table) resulting from SAM method applied on SWIR EO-1/Hyperion bands. The base image is a Laser Imaging Detection and Ranging digital terrain model artificially illuminated from northeast. (B) Reflectance spectrum extracted from point 1 (P.1) of EO-1/Hyperion imagery of (A), compared with a normalized kaolinite spectrum from USGS spectral library.

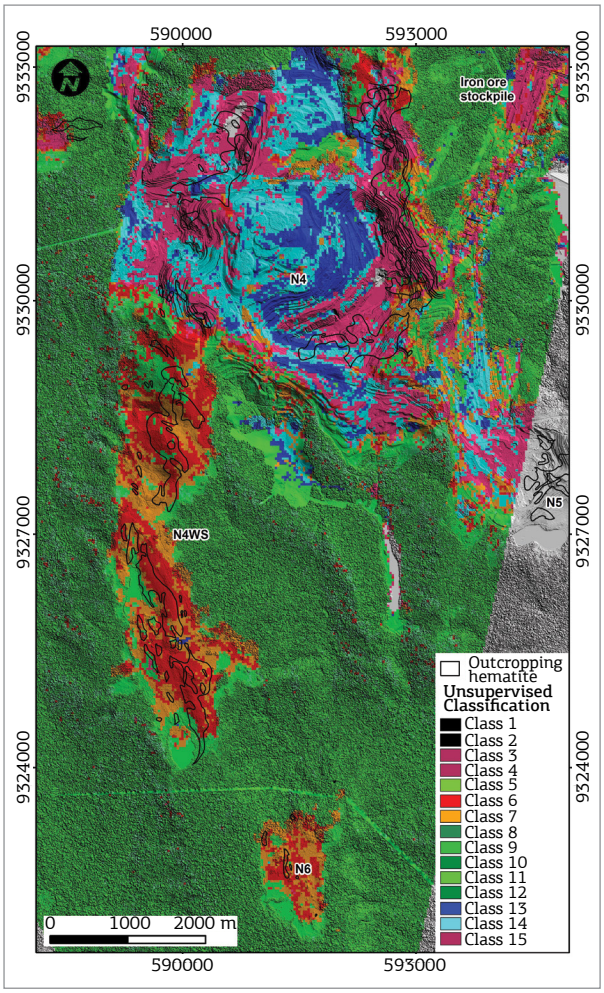

Figure 16. Class image resulting from unsupervised classification applied on Hyperion, gamma ray spectrometric data, Tzz gravimetric gradient component, and Landsat-8/OLI-derived Normalized Difference Vegetation Index data. The base image is a Laser Imaging Detection and Ranging digital terrain model artificially illuminated from northeast.

for Post-Doctorate (PNPD). A.M. Silva acknowledges the Brazilian National Counsel of Technological and Scientific Development (*Conselho Nacional de Desenvolvimento Científico e Tecnológico* – CNPq) for her research grant (Process 307177/2014-9). We also thank the Laboratory of Applied Geophysics of the Universidade de Brasília for technical support. We acknowledge the Commonwealth Scientific and Industrial Research Organisation (CSIRO) for its permission to use the MMTG A-List software. We are grateful for the detailed corrections, comments, and advice of Brazilian Journal of Geology Editor-in-Chief, Dr. Umberto Cordani, and Associate Editor, Alvaro P. Crósta, and also of two anonymous reviewers. We thank V.N. Ferreira for assistance on geophysical data, and M.F. Oyola for reviewing the manuscript.

REFERENCES

Abdelsalam M.G., Stern R.J., Berhane W.G. 2000. Mapping gossans in arid regions with Landsat TM and SIR-CIX-SAR images: The Beddaho alteration zone in northern Eritrea. *Journal of African Earth Sciences*, **30**(4):903-916.

Agar B. & Coulter D. 2007. Remote Sensing for Mineral Exploration – A Decade Perspective 1997-2007. *In:* Milkereit B. (ed.) *Proceedings of Exploration 07: Fifth Decennial International Conference on Mineral Exploration*, p.109-136.

Almeida T.I.R., Souza Filho C.R., Juliani C., Branco F.C. 2009. Application of Remote Sensing to Geobotany to Detect Hydrothermal Alteration Facies in Epithermal High Sulfidation Gold Deposits in the Amazon Region. *In:* Bedell R., Crósta A., Grunsky E. (eds.) *Remote Sensing and Spectral Geology*. SEG Special Publication, Society of Economic Geologists, 16, p. 135-142.

Assis L.M. 2013. *Geração de modelo exploratório para o minério de ferro da Província Mineral de Carajás através da integração de dados multifonte*. MS Dissertation, Instituto de Geociências, Universidade de Brasília, Brasília, 154 p.

Burns R. 1993. *Mineralogical Applications of Crystal Field Theory*. 2º ed. Cambridge, Cambridge University Press, 551 p.

Clark R.N. 1999. Chapter 1 - Spectroscopy of Rocks and Minerals, and Principles of Spectroscopy. *In:* Rencz A.N. (ed.) *Manual of Remote Sensing*. Remote Sensing for the Earth Sciences, New York, John Wiley and Sons, v. 3, p. 3-58.

Clark R.N. & Roush T.L. 1984. Reflectance spectroscopy: quantitative analysis techniques for remote sensing applications. *Journal of Geophysical Research*, **89**(B7):6329-6340.

Clark R.N., Swayze G.A., Wise R., Livo E., Hoefen T., Kokaly R., Sutley S.J. 2007. USGS digital spectral library splib06a. *U.S. Geological Survey, Digital Data Series*, 231. Available at: http://speclab.cr.usgs.gov/spectral.lib06. Cited in: 2016 Jan. 12.

Cloutis E.A., Gaffey M.J., Jackowski T.L., Reed K.L. 1986. Calibrations of phase abundance, composition, and particle size distribution for olivine-orthopyroxene mixtures from reflectance spectra. *Journal of Geophysical Research*, **91**:11641-11653.

Cordani U.G., Tassinari C.C.G., Teixeira W., Basei M.A.S., Kawashita K. 1979. Evolução tectônica da Amazônia com base nos dados geocronológicos. *In:* 2º Congresso Geológico Chileno, Arica, Chile, *Actas*, v. 4, p. 137-148.

Cudahy T. & Ramanaidou E.R. 1997. Measurement of the hematite:goethite ratio using field visible and near-infrared reflectance spectrometry in channel iron deposits, Western Australia. *Australian Journal of Earth Sciences*, **44**:411-420.

Datt B., McVicar T.R., Van Niel T.G., Jupp D.L.B., Pearlman J.S. 2003. Preprocessing EO-1 Hyperion Hyperspectral Data to Support the Application of Agricultural Indexes. *IEEE Transactions on Geoscience and Remote Sensing*, **41**(2):1246-1259.

DOCEGEO. 1988. *Revisão litoestratigráfica da Província Mineral de Carajás. In:* 35º Congresso Brasileiro de Geologia, Sociedade Brasileira de Geologia, Belém, Brazil, p. 11-54.

Farooq S. & Govil H. 2013. Mapping Regolith and Gossan for Mineral Exploration in the Eastern Kumaon Himalaya, India using hyperion data and object oriented image classification. *Advances in Space Research*, **53**(12):1676-1685.

Feizi F. & Mansouri E. 2013. Introducing the Iron Potential Zones Using Remote Sensing Studies in South of Qom Province, Iran. *Open Journal of Geology*, **3**(4):278-286.

Gibbs A.K., Wirth K.R., Hirata W.K., Olszewski W.S. 1986. Age and composition of the Grão Pará group volcanics, Serra dos Carajás. *Revista Brasileira de Geociências*, **16**(2):201-211.

Goetz A.F.H. & Rowan L.C. 1981. Geologic remote sensing. *Science*, **211**:781-791.

Goodenough D.G., Dyk A., Niemann K.O., Pearlman J.S., Chen H., Han T., Murdoch M., West C. 2003. Processing Hyperion and ALI for Forest Classification. *IEEE Transactions on Geoscience and Remote Sensing*, **41**(6):1321-1331.

Green A.A., Berman M., Switzer P., Craig M.D. 1988. A transformation for ordering multispectral data in terms of image quality with implications for noise removal. IEEE Transactions on Geoscience and Remote Sensing, **26**(1):65-74.

Hunt G.R. & Ashley R.P. 1979. Spectra of altered rocks in the visible and near-infrared: *Economic Geology*, **74**:1613-1629.

Hunt G.R., Salisbury J.W., Lenhoff C.J. 1971. Visible and near infrared spectra of minerals and rocks, III: Oxides and hydroxides. *Modern Geology*, **2**:195-205.

Knepper D.H. Jr. 1989. Mapping hydrothermal alteration with Landsat Thematic Mapper data. *In:* Lee K. (ed.). *Remote sensing in exploration geology — A combined short course and fieldtrip*. 28º International Geological Congress Guidebook T182, p. 13-21.

Kruse F.A., Lekhoff A.B., Dietz J.B. 1993. Expert system-based mineral mapping in northern Death Valley, California Nevada, using the airborne visible/infrared imaging spectrometer (AVIRIS). *Remote Sensing of Environment*, **44**:309-335.

Kruse F.A., Boardman J.W., Huntington J.F. 2003. Comparison of airborne hyperspectral data and EO-1 Hyperion for mineral mapping. *IEEE Transactions on Geoscience and Remote Sensing*, **41**(6):1388-1400.

Krymsky R.S., Macambira J.B., Macambira M.B.J. 2002. *Geocronologia U-Pb em zircão de rochas vulcânicas da Formação Carajás, Estado do Pará. In:* 2º Simpósio sobre vulcanismo e ambientes associados, Belém, Brazil, 41.

Lobato L.M., Rosière C.A., Figueiredo e Silva R.C., Zucchetti M., Baars F.J., Seoane J.C.S., Monteiro A.M. 2005. A mineralização hidrotermal de ferro da Província Mineral de Carajás-Controle estrutural e contexto na evolução metalogenética da província. *In:* Marini O.J., Queiroz E.T., Ramos B.W. (eds.) *Caracterização de depósitos minerais em distritos mineiros da Amazônia*. Brasília, DNPM-CT/MINERAL-ADIMB, cap. 2, p. 21-92.

Macambira J.B. 2003. *O ambiente deposicional da Formação Carajás e uma proposta de modelo evolutivo para a Bacia Grão Pará*. PhD Thesis, Instituto de Geociências, Universidade Estadual de Campinas, 217p.

Macambira J.B. & Schrank A. 2002. Químio-estratigrafia e evolução dos jaspilitos da Formação Carajás (PA). *Revista Brasileira de Geociências*, **32**: 567-578.

Mason P. 2002. *MMTG A-List Hyperspectral Data Processing Software*. 920C, CSIRO, Division of Exploration and Mining, Sydney, Australia, 103 p.

Mather P.M. 1999. *Computer Processing of Remotely-Sensed Images: An Introduction*. United Kingdom, John Wiley & Son Ltd, 2nd ed., 292 p.

Meirelles E.M., Hirata W.K., Amaral A.F., Medeiros Filho C.A., Gato W.C. 1984. Geologia das folhas Carajás e Rio Verde, Província Mineral de Carajás, Estado do Pará. *In:* 33º Congresso Brasileiro de Geologia, Rio de Janeiro, *Anais*, p. 2164-2174.

Morris R.V., Lauer H.V., Lawson C.A., Gibson E.K., Nace G.A., Stewart C. 1985. Spectral and other physicochemcial properties of submicron powders of hematite (alpha-Fe2O3), maghemite (gamma-Fe2O3), magnetite (Fe3O4), goethite (alpha-FeOOH) and lepidocrocite (gamma-FeOOH). *Journal of Geophysical Research-Solid Earth and Planets*, **90**:3126-3144.

Murphy C.A. 2004. The Air-FTG® airborne gravity gradiometer system. *In:* Lane R.J. (ed.). *Airborne Gravity 2004 – Abstracts from the ASEG-PESA Airborne Gravity 2004 Workshop*. Geoscience Australia Record, 18, p. 7-14.

Olszewski W.J., Wirth K.R., Gibbs A.K., Gaudette H.E. 1989. The age, origin, and tectonics of the Grão Pará Group and associated rocks. Serra dos Carajás, Brazil: Archean continental volcanism and rifting. *Precambrian Research*, **42**:229-254.

Paradella W.R., Bignelli P.A., Veneziani P., Pietsch R.W., Toutin T. 1997. Airborne and Spaceborne Synthetic Aperture Radar (SAR) Integration with Landsat TM and gamma ray spectrometry for geological mapping in a tropical environment, the Carajás Mineral Province, Brazil. *International Jouranl of Remote Sensing*, **18**(7):1483-1501.

Pearlman J.S., Barry P.S., Segal C., Shepanski J., Beiso D., Carman S. 2003. Hyperion, a space-based imaging spectrometer. *IEEE Transactions on Geoscience and Remote Sensing*, **41**:1160-1173.

Prado E.M.G., Silva A.M., Ducart D.F., Toledo C.L.B., Assis L.M. 2016. Reflectance spectroradiometry applied to a semi-quantitative analysis of the mineralogy of the N4ws deposit, Carajás Mineral Province, Pará, Brazil. *Ore Geology Reviews*, **78**:101-119.

Ramanaidou E., Wells M., Belton D., Verrall M., Ryan C. 2008. Mineralogical and Microchemical Methods for the Characterization of High-Grade Banded Iron Formation-Derived Iron Ore. *In:* Hagemann S., Rosière C.A., Gutzmer J., Beukes N.J. (eds.) *Banded Iron Formation-related High-grade Iron Ore*. Society of Economic Geologists, 15, p. 129-156.

Resende N.P. & Barbosa A.L.M. 1972. *Relatório de Pesquisa de Minério de Ferro, Distrito Ferrífero da Serra dos Carajás, Estado do Pará*. AMZA, Relatório Final de Pesquisa, v.1, texto, 248 p, v.2, mapas e seções geológicas, p. 119.

Rockwell B.W. 2013. Automated mapping of mineral groups and green vegetation from Landsat Thematic Mapper imagery with an example from the San Juan Mountains, Colorado. *U.S. Geological Survey Scientific Investigations Map 3252*, pamphlet, 1 map sheet, scale 1:325,000, 25 p.

Rowan L., Wetlaufer P., Goetz A., Billingsley F., Stewart J. 1974. Discrimination of rock types and detection of hydrothermally altered areas in south-central Nevada by the use of computer-enhanced ERTS images. *U.S. Geological Survey Professional Paper*, 883, 35 p.

Santos J.O.S. 2003. Geotectônica dos Escudos da Guianas e Brasil-Central. *In:* Bizzi L.A., Schobbenhaus C., Vidotti R.M., Gonçalves J.H. (eds.). *Geologia, Tectônica e Recursos Minerais do brasil*. Companhia de Pesquisa e Recursos Minerais-CPRM, p. 169-226.

Santos J.O.S., Hartmann L.A., Gaudette H.E., Groves D.I., McNaughton N.J., Flecher I.R. 2000. New understanding of the Amazon Craton provinces, based on field work and radiogenic isotope data. *Gondwana Research*, **3**(4):453-488.

Santos J.O.S., Hartmann L.A., Faria M.S., Riker S.R., Souza M.M., Almeida M.E., McNaughton N.J. 2006. *A compartimentação do Cráton Amazonas em províncias: avanços ocorridos no período 2000-2006. In:* 9º Simpósio de Geologia da Amazônia, Sociedade Brasileira de Geologia, Belém, Brazil, *Resumos Expandidos*, CD ROM.

Sherman D.M. & Waite T.D. 1985. Electronic spectra of Fe3+ oxides and oxide hydroxides in the near IR to near UV. *American Mineralogist*, **70**:1262-1269.

Singer R.B. 1981. Near-infrared spectral reflectance of mineral mixtures – Systematic combinations of pyroxenes, olivine, and iron oxides. *Journal of Geophysical Research*, **86**:7967-7982.

Silva M.F.F., Secco R.S., Lobo M.G.A. 1996. Aspectos ecológicos da vegetação rupestre da Serra dos Carajás, estado do Pará, Brasil. *Acta Amazonica*, **26**:17-44.

Tallarico F.H.B., McNaughton N.J., Groves D.I., Fletcher I.R., Figueiredo B.R., Carvalho J.B., Rego J.L., Nunes A.R. 2003. Geological and SHRIMP II U-Pb constraints on the age and origin of the Breves Cu-Au-(W-Bi-Sn) deposit, Carajás, Brazil. *Mineralium Deposita*, **39**:68-86.

Tassinari C.C.G. & Macambira M.J.B. 1999. Geochronological provinces of the Amazonian Craton. *Episodes*, **22**:174-182.

Tassinari C.C.G. & Macambira M.J.B. 2004. A evolução tectônica do Cráton Amazônico. *In:* Mantesso-Neto V., Bartorelli A., Carneiro C.D.R., Brito Neves B.B. (eds.) *Geologia do Continente Sul-Americano: Evolução da Obra de Fernando Flávio Marques de Almeida*. São Paulo, BECA, p. 471-485.

Tassinari C.C.G., Bettencourt J.S., Geraldes M.C., Macambira M.J.B., Lafon J.M. 2000. The Amazonian Craton. *In:* Cordani U.G., Milani E.J., Filho A.T., Campos D.A. (eds.) *Tectonic Evolution of South America*. Rio de Janeiro, International Geological Co., p. 41-95.

Trendall A.F., Basei M.A.S., de Laeter J.R., Nelson D.R. 1998. Ion microprobe zircon, U-Pb results from the Carajás area of the Amazon Craton. *Journal of South American Earth Sciences*, **11**:265-276.

Tolbert G.E., Tremaine J.W., Melcher G.C., Gomes C.B. 1971. The recently discovered Serra dos Carajás iron deposits, Northern Brazil. *Economic Geology*, **7**:985-994.

Tou J.T. & Gonzalez R.C. 1974. *Pattern Recognition Principles*. New York, Addison-Wesley, Reading, MA, 377 p.

Townsend T.E. 1987. Discrimination of iron alteration minerals in visible and near-infrared reflectance data. *Journal of Geophysical Research-Solid Earth and Planets*, **92**:1441-1454.

VALE. 2015. *Annual Report - Resource and Reserve Statement 2014, Vale – Iron Ore*. Belo Horizonte, Brazil. 30 p.

White K., Walden J., Drake N., Eckardt F., Settle J. 1997. Mapping the iron oxide content of dune sands, Namib Sand Sea, Namibia, using Landsat Thematic Mapper data. *Remote Sensing of Environment*, **62**:30-39.

Wirth K.R., Gibbs A.K., Olzewski Jr. W.J. 1986. U-Pb zircon ages of the Grão Pará Group and Serra dos Carajás granite. *Revista Brasileira de Geociências*, **16**:195-200.